Cellulose (2023) 30:7177–7191
https://doi.org/10.1007/s10570-023-05325-2

ORIGINAL RESEARCH

One-dimensional nanostructured vanadium oxides with single-crystalline structure synthesized by cellulose nanocrystal-template-assisted hydrothermal method for Li-ion battery cathodes

Chulmin Youn · Wonseok Ko · Ayoung Cho · Joonbong Lee · Sang Young Yeo · Yongho Seo · Jonghun lee · Byoung-Sun Lee · Jongsoon Kim · Taekjib Choi

Received: 27 June 2022 / Accepted: 12 June 2023 / Published online: 26 June 2023

Abstract Cellulose nanocrystals (CNCs) have emerged as a promising templating material due to unique features, such as high surface area, surface hydroxyl groups and rod-like shape, which allow for sustainable nanoscale control of advanced functional materials. Especially, such high surface functionality and specific morphology can be imparted on the resultant nanomaterials with beneficial properties during templating. Here, we present synthesis of one-dimensional (1D) nanostructured vanadium oxides, such as VO_2(B) and $V_2O_5{\cdot}nH_2O$ nanobelts, with single- crystalline structure by hydrothermal treatment using CNCs as a sacrificial template. Importantly, the single-crystal vanadium oxide nanobelts exhibit the enhanced electrochemical performance of Li ion batteries with high specific capacity (> 300 mAh/g) and long lifespan (> 244 mAh/g at 50 cycles) compared to

Supplementary Information The online version contains supplementary material available at https://doi.org/10.1007/s10570-023-05325-2.

C. Youn · S. Y. Yeo
Bio-Convergence Research Center, Korea Textile Machinery Convergence Research Institute, 27 Sampung-ro, Gyeongsan-City, Gyeongbuk 38542, Republic of Korea

C. Youn · A. Cho · J. Lee · Y. Seo · T. Choi (✉)
Hybrid Materials Research Center, Department of Nanotechnology and Advanced Materials Engineering, Sejong University, 209 Neungdong-ro, Gwangjin-gu, Seoul 05006, Republic of Korea
e-mail: tjchoi@sejong.ac.kr

W. Ko · J. Kim (✉)
Department of Energy Science, Sungkyunkwan University, 2066 Seobu-ro, Jangan-gu, Suwon-si, Gyeonggi-do 16419, Republic of Korea
e-mail: jongsoonkim@skku.edu

W. Ko · J. Kim
SKKU Institute of Energy Science and Technology (SIEST), Sungkyunkwan University, 2066 Seobu-ro, Jangan-gu, Suwon-si, Gyeonggi-do 16419, Republic of Korea

S. Y. Yeo
Advanced Textile R&D Department, Korea Institute of Industrial Technology, 143 Hanggaul-ro, Ansan-si, Gyeonggi-do, Republic of Korea

J. lee
Division of Automotive Technology, Daegu Gyeongbuk Institute of Science and Technology, 333 Techno Jungang-daero, Hyeonpung-eup, Dalseong-gun, Daegu 42988, Republic of Korea

J. lee
Department of Interdisciplinary Engineering, Graduate School, Daegu Gyeongbuk Institute of Science and Technology, 333 Techno Jungang-daero, Hyeonpung-eup, Dalseong-gun, Daegu 42988, Republic of Korea

B.-S. Lee (✉)
School of Polymer System/Department of Fiber Convergence Material Engineering, College of Engineering, Dankook University, 152 Jukjeon-ro, Suji-gu, Yongin-si, Gyeonggi-do 16890, Republic of Korea
e-mail: bslee2020@dankook.ac.kr

the polycrystalline nanoflakes counterpart. Furthermore, we suggest that during hydrothermal treatment the sacrificial CNC template-derived carbon is beneficial for electron transfer in cathode materials. Thus, we demonstrate that the utilization of CNC templating to develop novel single-crystalline oxide cathode nanomaterials can provide a fruitful pathway for extraordinary electrochemical performance of next-generation alkaline batteries.

Keywords Cellulose nanocrystal · Sacrificial template · Hydrothermal treatment · Single-crystalline nanostructured vanadium oxides · Li ion battery cathode

Introduction

Control over the microstructure and specific morphology of nanostructures is the most important benefit of templating to confer beneficial properties on the resultant materials (Lamm et al. 2021; Yang et al. 2021). Recently, nanocellulose, including cellulose nanofibers (CNFs) and cellulose nanocrystals (CNCs), as a renewable and naturally abundant nanoscale template, has attracted significant research interest in the synthesis of advanced functional nanomaterials for next-generation energy applications (Moon et al. 2011; Youn et al. 2022; Xu et al. 2021). In general, nanocellulose exhibits a number of unique properties such as the anisotropic shape, the large specific surface area and the controllable surface chemistry (Eyley and Thielemans 2014; Merindol et al. 2020; Yamaguchi et al. 2012). The highly crystalline nanocellulose also offers a rigid surface with tunable functional groups (De France et al. 2021). In particular, the presence of abundant hydroxyl (OH^-) groups on the surface of nanocellulose allows potential chemical modifications to develop viable and facile routes for eco-friendly nanocomposites or functional nanomaterials in various energy applications such as high performance catalysis and energy storage (Wang et al. 2017; Youn et al. 2021). However, it is a challenge to prepare functional nanomaterials with the corresponding morphological hierarchies of the natural species. The CNFs can easily generate foams due to their intrinsic high water retention, which promotes foaming, the foams have a high surface area and a porous structure with pores of different lengths (Lavoine and Bergström 2017; Lin et al. 2012). The CNFs also form interconnected fiber networks due to their long fiber morphology and can support more complex morphologies during the templating process. Rod-shaped CNCs possess a high crystallinity and a high aspect ratio with average diameter of 5–20 nm and average length of 100–200 nm, making them an ideal template for the preparation of crystalline material (Moon et al. 2011). Thus, by employing nanocellulose as an intermediate or sacrificial templates, the fabrication of various metal oxides and silicon-based nanocomposites with excellent electrochemical properties can provide a sustainable way to develop novel Li ion batteries (LIBs) as they enable the growth of tubular and rod-shaped nanostructure of electrode materials resulting from their unique properties and the synergistic effects of composite components. On the other hand, it has been successfully applied to nanocellulose to obtain the corresponding nanomaterials through the following calcination or carbonization processes, which imparted the unique hierarchically porous network structures and specific properties (Liu et al. 2019).

LIBs have been successfully used as portable power sources for applications ranging from small electronic devices to electric vehicles due to their high capacity, long life, and low self-discharge (Chen et al. 2019; Wu et al. 2014). Despite the excellent electrochemical performance of current LIBs, the demand for even higher energy densities and improved performance for many applications is still growing rapidly. Enormous efforts have been expended to develop novel energy storage materials and systems to meet these needs, and novel cathode materials have been extensively explored since the electrochemical performance is mainly determined by the cathode materials (Fan et al. 2016; Xu et al. 2012). Traditional lithium-metal oxide and phosphate cathode materials such as $LiCoO_2$ (LCO) with layered structure and olivine-structured $LiFePO_4$ (LFP) have been used due to their structural stability during the electrochemical reactions (Chen et al. 2019; Fan et al. 2016; Kramer and Ceder 2009; Lee et al. 2014; Rahman et al. 2010). However, their inherent low specific capacities in the normal operation potential range (2.5–4.5 V) have motivated the design of layered oxide cathode materials ($LiNi_xCo_yMn_zO_2$ (NCM)) with high nickel content for improved specific capacities (> 200 mAh/g) (Susai et al. 2018) and energy density (300 Wh/kg)

(Qiao et al. 2020), with some NCM cathode materials being successfully used in commercial LIBs (Chen and Zhu 2019; Jeon and Baek 2011). Despite these achievements, further improvement in the specific capacity of cathode materials is needed, and the morphologies and structures of cathode materials are crucial for practical LIBs. Although these cathode materials with different nanostructures have been reported to exhibit superior electrochemical performance, among the various forms of these materials, single-crystal cathodes (SCs) have demonstrated many advantages over their polycrystalline counterparts for industrial applications, including high crystallinity, high mechanical strength, homogeneous response, small specific surface area, high structural stability, which can suppress cracking, side reactions and gas release, improving overall cycle performance and thermal stability (Kimijima et al. 2016; Chen et al. 2019; Xu et al. 2019). Hence, it is crucial to develop novel single-crystal cathode nanomaterials with high specific capacity and long cycle performance for next-generation LIBs.

Vanadium oxides are considered promising candidates because of their intriguing material properties based on multiple oxidation states (V^{2+} to V^{5+}), such as a metastable chemical structure and a two-dimensional layered crystal structure (He et al. 2015; Li et al. 2011; Livage 2010; Zhao et al. 2015). In addition, there is a wide variety of vanadium oxide structures in terms of stoichiometry (e.g., V_2O_5, V_2O_3, VO_2, and V_6O_{13}) and polymorphism (e.g., VO_2(A), VO_2(B), VO_2(M), and VO_2(R)) (Bahlawane and Lenoble 2014; He et al. 2015; Lee et al. 2016; Li et al. 2011; Liu et al. 2009; Zhang et al. 2021). Among the various vanadium oxides, VO_2(B) is an attractive candidate for alternative cathode applications owing to its high specific capacity (~320 mAh/g) and wide working potential window (from 1.0 to 4.0 V vs. Li/Li^+) (Chen et al. 2019; Fan et al. 2016; Liang et al. 2013; Liu et al. 2009; Lübke et al. 2016). The facile Li-ion diffusion in the VO_2(B) crystal structures resulting from the two-dimensional layered structure with corner sharing of the VO_6 octahedra is also beneficial for high-performance LIBs (Li et al. 2017). Hydrated vanadium oxide ($V_2O_5{\cdot}nH_2O$) is another promising candidate with a specific capacity of (300 mAh/g) and structural advantages (interlayer spacing of 8.8 to 13.8 Å) for Li-ion conduction (Sudant et al. 2004; Sun et al. 2021; Wang et al. 2005; Wei et al. 2015; Zhao et al. 2019). Therefore, it is expected that the identification of an effective means to synthesize 1D nanostructured vanadium oxides (NVOs) given the cathode nanomaterials can help accelerate the development of next-generation LIBs with high energy density, short ion diffusion paths, and electronic conduction (Liu et al 2017b; Prześniak-Welenc et al 2016; Saji et al 2011; Zhao et al 2015). Furthermore, the availability of a single-phase synthesis for high-performance LIB cathodes is crucial to prevent uncontrollable electrochemical behavior resulting from the polymorphism of the vanadium oxides. In this work, $V_2O_5{\cdot}nH_2O$ and VO_2(B) NB with excellent electrochemical performance were designed using a crystal structure selective synthesis method for a 1D nanostructure based on a hydrothermal process and a 2,2,6,6-tetramethylpiperidine-1-oxyl (TEMPO) oxidation-treated cellulose nanocrystal (TCNC) templating. Previous studies have shown that producing single crystal VO_2(B) or $V_2O_5{\bullet}nH_2O$ through the hydrothermal synthesis process requires a lengthy reaction time of more than 4 days. However, by employing the cellulose nanocrystal template, it is possible to obtain a highly crystalline final product within a short period of time (Subba Reddy et al. 2009; Wang et al. 2019). To the best of our knowledge, there are no reports of a 1D inorganic nanostructure obtained by using a TCNCs as a template. The morphological, structural, and electrochemical properties of single crystalline $V_2O_5{\cdot}nH_2O$ and VO_2(B) NBs have been thoroughly and systematically studied to demonstrate the feasibility of these materials as next-generation single-crystal cathode materials.

Experimental

Preparation of the TEMPO-oxidized cellulose nanocrystals

The 3.05 wt% cellulose nanofiber slurry (University of Maine, 5 g) was dispersed in DI water (200 ml) by stirring at 600 rpm at room temperature. Then, TEMPO (Sigma Aldrich, 98%, 0.03 g) and NaBr (Sigma Aldrich, ACS reagent, 0.3 g) were added to the cellulose fiber solution (a white suspension) and completely dissolved for 30 min to obtain an ivory solution (Okita et al. 2010; Shinoda et al. 2012).

The NaClO solution (Duksan Chemical, Extra pure, 35%, 7 ml) was slowly added in 1 ml increments each 30 min, and after 24 h, a clear yellow solution was obtained. The pH was maintained at 10.5 by adding 0.5 M NaOH (Sigma Aldrich, ACS reagent) to the yellow solution, and the solution gradually became transparent. The high pH of the reacted solution was neutralized to pH 7 with the addition of 0.1 M HCl (Sigma Aldrich, ACS reagent). To obtain TCNCs that were completely dispersed in solution, ethanol was added to aggregate. The resulting final product (6.45 wt% of TCNCs) was obtained in gel form using a centrifuge (12,000 rpm, 10 min.) (Fig. S1).

Synthesis of the nanostructured vanadium oxides

The nanostructured vanadium oxides (NVOs) were synthesized by a hydrothermal synthesis according to the conditions shown in Table 1. In this hydrothermal synthesis, the morphology and crystal structure of vanadium oxide depend on the content of TCNCs and the process temperature. Polycrystalline VO_2(B) NFs were hydrothermally synthesized without TCNCs add to the precursor. $V_{10}O_{24}{\cdot}12H_2O$, $V_2O_5{\cdot}nH_2O$, VO_2(B) and amorphous phase were synthesized depending on the amount of TCNCs in the precursor. Unlike other vanadium oxides, highly crystalline VO_2(B) is hydrothermally synthesized at a process temperature of 250 °C.

The hydrothermal synthesis is performed in the following order (Figure S2). Each dose of 6.34 wt% TCNCs in gel form was added to 100 mL of deionized water, a completely dispersed and transparent solution was obtained. 18.6 mg of vanadium pentoxide (Sigma Aldrich) was dissolved for 30 min using magnetic stirrer. When the color of the solution turned dark yellow because of the well-dissolved V_2O_5, 31.6 mg of citric acid monohydrate (Sigma Aldrich, ACS reagent) was added, and the solution was further stirred for 30 min. The resulting product was transferred to a Teflon-lined stainless-steel autoclave. The sealed steel autoclave was heated at 180 °C for 1 h using a furnace and reacted continuously at 220 or 250 °C for 4 h (Popuri et al. 2013). The as-prepared solution was exfoliated in a sonication bath for 1 h and filtered with deionized water to obtain a film.

Table 1 Vanadium oxide nanostructure prepared by hydrothermal synthesis under various conditions

Crystal structure	TCNCs (g)	Temperature (℃)
VO_2(B) NFs	0	220
$V_{10}O_{24}{\cdot}12H_2O$ NWs	0.1	220
$V_2O_5{\cdot}nH_2O$ NBs	0.4	220
VO_2(B) NBs	0.4	250
VO_2(B) NRs	0.8	220
Amorphous phase NPs	1.0	220

Material characterization

All crystal structure and information were analyzed using X-ray diffraction (XRD; Rigaku) with Cu Kα radiation ($\lambda = 1.54178$ Å), and structural data were collected over the 2θ range of 10°–50° and 10°–60°. Rietveld refinement of polycrystalline VO_2(B) and profile matching of single crystalline VO_2(B) and $V_2O_5{\cdot}nH_2O$ were performed based on the Inorganic Crystal Structure Database (ICSD) such as VO_2 (ICSD #250,831) and $V_2O_5(H_2O)$ (ICSD #94,905) using FullProf software and the background of each XRD pattern was established using the 'Linear interpolation between a set of background points with refinable heights' option in FullProf software. The microstructure image of each sample was examined using field-emission scanning electron microscopy (FESEM; Hitachi) at an accelerating voltage of 15 kV and high- resolution transmission electron microscopy (HRTEM; JEOL) at an accelerating voltage of 200 kV. Raman spectra were obtained using a inVia (Renishaw; $\lambda = 514.5$ nm). Chemical bonding of V and C were analyzed by X-ray photoelectron spectroscopy (XPS; ThermoFisher Scientific).

Electrochemical characterization and preparation of battery button cells

Electrochemical tests were performed using CR2032-type button cells assembled in an Ar-filled glovebox. To prepare the electrodes, the samples were combined with Super P (carbon black) and polyvinylidene fluoride (PVDF) in a weight ratio of 8:1:1 in *N*-methyl-2-pyrrolidone (NMP). The prepared slurry was cast onto Al foil and dried at 80 °C overnight to remove the NMP. After drying, circular disks of 10-mm diameter were punched out. The mass loading of the active material was 4 mg/cm^2. The cell was

assembled using Li metal as the counter electrode, a separator (Whatman GF/F glass fiber), and electrolyte solution (1.2 M $LiPF_6$ in a 3:7 volume ratio of ethylene carbonate (EC): dimethyl carbonate (DMC) and 3% of vinylene carbonate (VC)). Galvanostatic charge/discharge tests were performed at 1C (1C corresponds to 323.19 mAh g^{-1}) for VO_2 using an automatic battery test system (WBCS 3000, WonATech).

Results and discussion

The structural characterization of nanostructured vanadium oxides

The NVOs with low dimensions such as nanoparticles (NPs), nanorods (NRs), nanobelts (NBs), and nanosheets (NSs) have been extensively studied for energy applications due to their remarkable catalytic activities and excellent interactions with ions. It is high desirable for achieving NVOs with controllable morphology and high-quality single crystalline. The hydrothermal process can effectively synthesize such NVOs with various morphologies, sizes and crystalline phases influenced by controlling the parameters, e.g. reaction temperature, time and the nature of the reducing agent during the synthesis process.

The hydrothermal synthesis process is as follows (Figure S3). When the raw V_2O_5 particles were dissolved in distilled water, metal cations (V^{5+}) were hydrated to form $V_2O_5 \bullet nH_2O$. Adding citric acid monohydrate to the hydrated V_2O_5 resulted in two equivalents of vanadic acid (H_3VO_4). The vanadic acid was then decomposed into VO_2^+, OH^-, and H_2O molecules under high temperature and pressure. The VO_2^+ was assembled and nucleated through the electrical attraction between multivalent vanadium cations (e.g., V^{3+}, V^{4+} and V^{5+}) and electronegative molecules (e.g., –OH of H_2O or –COONa of TCNCs). Then, in the first-stage hydrothermal synthesis, metastable monoclinic crystals were grown at a reaction temperature of 180 °C. Additional thermal energy was used for the following serial reaction steps: (i) partial reduction and hydration, (ii) full reduction and hydration, and (iii) dehydration (Popuri et al. 2013).

A 1D and chemically treated biomass TCNC-templated hydrothermal process has been newly developed to synthesize NVOs (Youn et al. 2022). The crystalline phases and morphologies of NOVs synthesized by TCNC-templated hydrothermal synthesis strongly depend on the TCNC contents and the process temperatures, as shown schematically in Fig. 1. Note that the polycrystalline VO_2(B) NFs were obtained under typical hydrothermal conditions without TCNCs.

The crystalline structure and morphology of the as-prepared NVOs were characterized by X-ray diffraction (XRD), field emission scanning electron microscopy (FESEM), high-resolution transmission electron microscopy (HRTEM), and Raman spectroscopy. As shown in Fig. 2, XRD analysis shows the crystalline phase evolution in vanadium oxides as a function of TCNC contents (0.0–1.0 g) and processing temperatures (220 °C and 250 °C). We observed

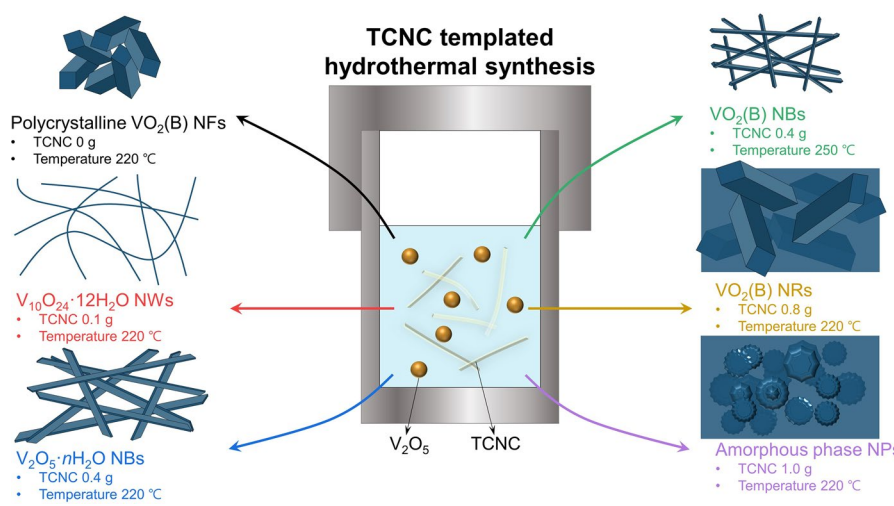

Fig. 1 The schematic diagram of the different morphologies and crystalline phases for nanostructured vanadium oxides synthesized through TCNC-templated hydrothermal method according to the TCNC amounts and process temperatures

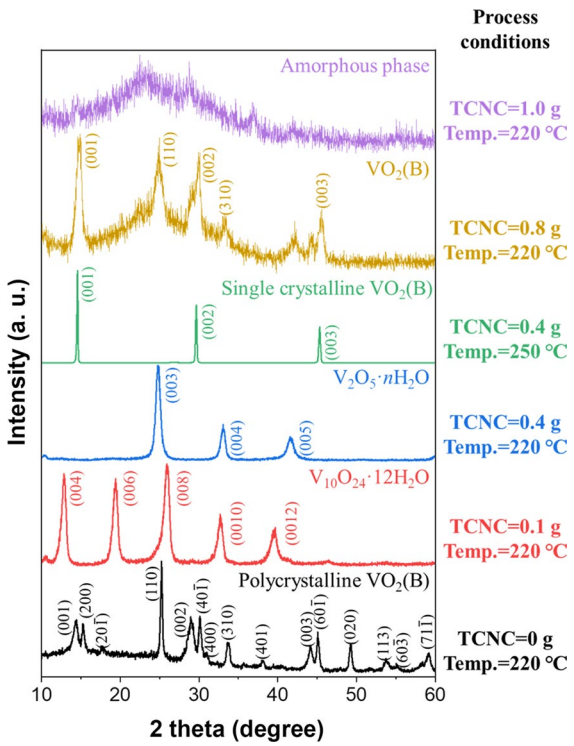

Fig. 2 XRD analysis of vanadium oxides with various process conditions through TCNC templated hydrothermal synthesis; black: polycrystalline VO_2(B), red: $V_{10}O_{24}{\cdot}12H_2O$, blue: $V_2O_5{\cdot}nH_2O$, green: single crystalline VO_2(B), yellow: VO_2(B), violet: amorphous phase

a transition from $V_{10}O_{24}{\cdot}12H_2O$ to VO_2(B) with the formation of the intermediate $V_2O_5{\cdot}nH_2O$ through a reduction−dehydration process. When TCNCs were not added, polycrystalline VO_2(B) was synthesized, and this was confirmed through Rietveld refinement based on the XRD pattern (Fig. S4, Table. S1 and S2) with reliable R-factors of $R_p = 5.32\%$, $R_{wp} = 7.01\%$, $R_{exp} = 2.015\%$, $R_I = 7.00\%$, $R_F = 2.34\%$ and $\chi^2 = 12.10\%$. Generally, each of the R-factors R_p, R_{wp}, R_{exp}, R_I, and R_F represent the profile R-factor, weighted profile R-factor, expected profile R-factor, Bragg R-factor, and structure R-factor, respectively and the value of χ^2 indicates a good fit of the profile, calculated as the square of R_{wp} divided by R_{exp} (Toby. 2006; Salah et al. 2019). In case of adding a small amount of TCNCs (0.1 g and 0.4 g), the layer structured hydrated vanadium oxides were formed, showing a set of only (00 *l*) diffraction peaks (Ahmed et al. 2019; Petkov et al. 2002). Interestingly, when a higher processing temperature (250 °C), we obtained the single crystalline VO_2 (B) with the sharp (00 *l*) reflections, indicative of complete dehydration. Moreover, as shown in Fig. S5 and Fig. S6, we confirmed that when 0.4 g of TCNCs was added and the processing temperature was 220 or 250 °C, the XRD patterns showed formed single crystals of $V_2O_5{\bullet}nH_2O$ and VO_2(B), respectively, which were confirmed by profile matching using the Fullprof (Li et al. 2006, 2011; Liu et al. 2017a). The Bragg positions, which appear except for the main peak in the XRD pattern, may be attributed to the metastable characteristics of vanadium oxide. They are considered negligible since they may have originated from either the starting material (V_2O_5) or by-products with different stoichiometry. On the other hand, when TCNCs excess content was added, polycrystalline vanadium oxide or an amorphous product was synthesized.

Figure 3 shows the various morphologies of NVOs prepared under different hydrothermal synthesis conditions. Vanadium oxides were synthesized into nanostructures with different aspect ratios depending

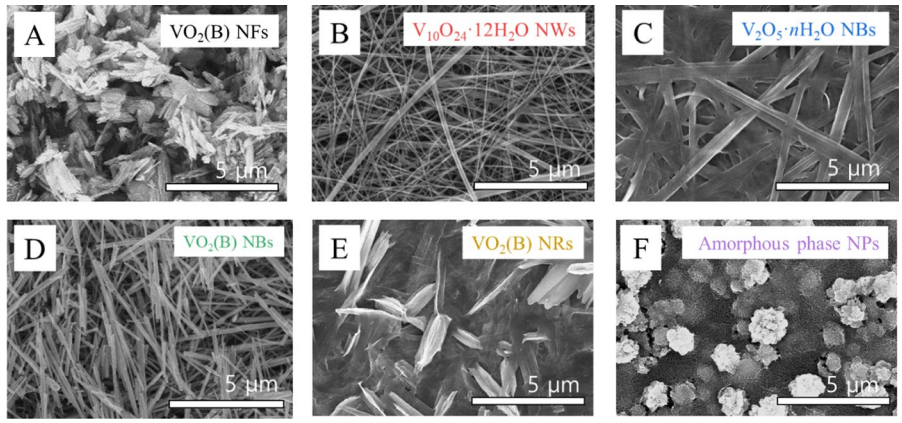

Fig. 3 FESEM images of NVOs with different morphology and crystal phases: **a** polycrystalline VO_2(B) NFs, **b** $V_{10}O_{24}{\cdot}12H_2O$ NWs, **c** $V_2O_5{\cdot}nH_2O$ NBs, **d** VO_2(B) NBs, **e** VO_2(B) NRs, and **f** amorphous phase NPs

on the addition amount of TCNCs during the hydrothermal process. It is worth noting that TCNCs as a template can provide primary reactive sites such as carboxyl (COOH–) and hydroxyl (OH–) groups that impart stable negative electrostatic charges on the surface to attract the dissolved metal ions. During the hydrothermal reaction, the metal ions confined by TCNCs template turned into nanostructures. As the amount of TCNCs added to the precursor increased, the aspect ratio gradually decreased with morphological change of NWs → NBs → NRs → NPs. Due to the aggregation of excess TCNCs in the process of forming vanadium oxide, a polycrystalline or amorphous crystal structure with a low aspect ratio is synthesized.

The detailed crystal structures of the $V_2O_5{\cdot}nH_2O$ and VO_2(B) NBs were investigated by using HRTEM, as shown in Fig. 4. The average length and width of the $V_2O_5{\cdot}nH_2O$ NBs were measured to be approximately 50 μm and 180 nm, respectively, and the aspect ratio was calculated as 1:278 (refer to Fig. S7a). The average length and width of the VO_2(B) NBs were shorter (~ 20 μm) and thinner (120 nm) than those of the $V_2O_5{\cdot}nH_2O$ NBs, and the aspect ratio was calculated to be 1:167 (refer to Fig. S7b). The reduced dimensions and aspect ratio of the VO_2(B) NBs result from complete reduction, dehydration, and subsequent structural densification at high processing temperature (250 °C). The low-magnification HRTEM images of both the $V_2O_5{\cdot}H_2O$ and VO_2(B) NBs (Fig. 4a, b) show the typical 1D single-crystalline nanostructure. Notably, the TCNC templates are not observed in the $V_2O_5{\cdot}nH_2O$ and VO_2(B) NBs. However, it is clear that the 1D nanostructures are derived from the TCNC templates. It could be understood that the TCNC templates were thermally decomposed during the hydrothermal process (Sevilla and Fuertes 2009). Figure 4c, d show the high-magnification HRTEM images of the $V_2O_5{\cdot}nH_2O$ and VO_2(B)

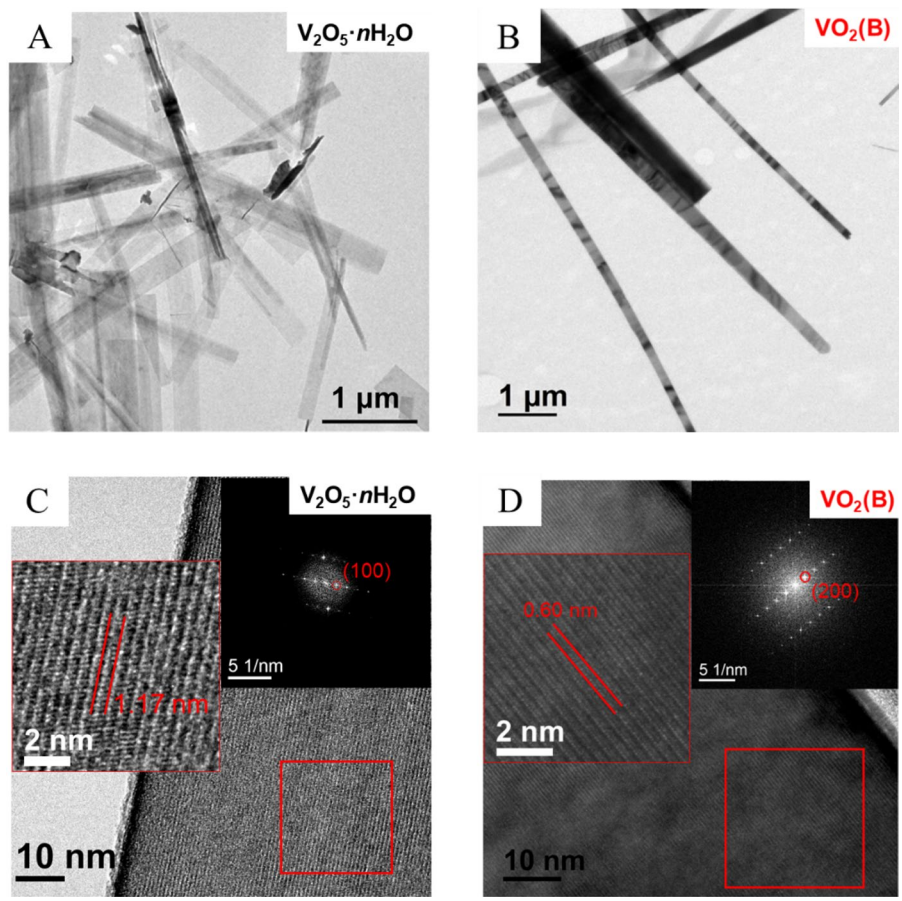

Fig. 4 Low-magnification HRTEM images for **a** $V_2O_5{\cdot}nH_2O$ and **b** VO_2(B) NBs. High-magnification HRTEM images for **c** $V_2O_5{\cdot}nH_2O$ and **d** VO_2(B) NBs. The left and right insets are zoom-in HRTEM images and corresponding FFT images in red lined boxes of figures c and d, respectively

NBs, respectively, and the insets illustrate zoom-in HRTEM images and corresponding the fast Fourier transform (FFT) images showing the well-defined single crystalline lattices. The lattice spacing of the $V_2O_5{\cdot}nH_2O$ and VO_2(B) NBs were measured to be 1.17 and 0.60 nm, which correspond to the distance between two (100) crystal planes, respectively, indicating the whole NBs are single crystal. Note that the crystal structure of the $V_2O_5{\cdot}nH_2O$ and VO_2(B) have a space group of C 12/m1 (Li et al. 2006, 2011; Liu et al. 2017a). It could be concluded that the 1D-template-based hydrothermal process enables the synthesis of the single crystalline 1D nanostructure with preferred orientations.

The chemical compositions and structures of the $V_2O_5{\cdot}nH_2O$ and VO_2(B) NBs were investigated using Raman spectroscopy and X-ray photoemission spectroscopy (XPS) (Fig. 5). It reveals that the $V_2O_5{\cdot}nH_2O$ NBs mainly consist of triply and doubly coordinated oxygen (V_3–O and V_2–O) stretching modes and exhibit the D and G peaks of the carbonaceous structure at approximately 1350 and 1580 cm^{-1}, which are attributed to the incomplete thermal decomposition of the TCNCs because of the lower hydrothermal process temperature (220 °C) (Ferrari and Robertson 2000; Lazzarini et al. 2016). In contrast, for VO_2(B) NBs, the V=O and V–O–O peaks were primarily developed (Arcangeletti et al. 2007; Perera et al. 2011; Wang et al. 2014; Zhang et al. 2009), and the carbonaceous-structure-driven D and G peaks did not appear because of the complete thermal decomposition of the TCNCs at the high hydrothermal process temperature (250 °C) (Sevilla and Fuertes 2009).

We compared quantitative analyses of the atomic compositions for the $V_2O_5{\cdot}nH_2O$ and VO_2(B) NBs by X-ray photoemission spectroscopy (XPS) analysis. Figure 5b, c present the $V2p_{3/2}$ spectra of the $V_2O_5{\cdot}nH_2O$ and VO_2(B) NBs. Note that the evaluation of the oxidation state of vanadium by analyzing the $V2p_{3/2}$ core-level binding energy provides information on the crystallographic structures of vanadium oxides (Kang et al. 2019; Li et al. 2013b). The $V2p_{3/2}$ spectrum of the $V_2O_5{\cdot}nH_2O$ NBs was deconvoluted into V^{4+} (20%) at 516 eV and V^{5+} (80%) at 517 eV (Hu et al. 2019; Simões et al. 2015; Wei et al. 2015), whereas that of the VO_2(B) NBs was simply assigned to V^{4+}. The predominant V^{5+} and V^{4+} peaks in the $V2p_{3/2}$ spectra were well-matched to the crystallographic structures of the $V_2O_5{\cdot}nH_2O$ and VO_2(B) NBs. High-resolution C1s spectra of the $V_2O_5{\cdot}nH_2O$ and VO_2(B) NBs may be attributed to the residual thermally decomposed TCNC templates, as shown in Fig. S8a and S8b, respectively. Because of the incomplete thermal decomposition of the TCNCs, the high-resolution C1s spectrum intensity of the $V_2O_5{\cdot}nH_2O$ NBs was much higher than that of the VO_2(B) NBs,

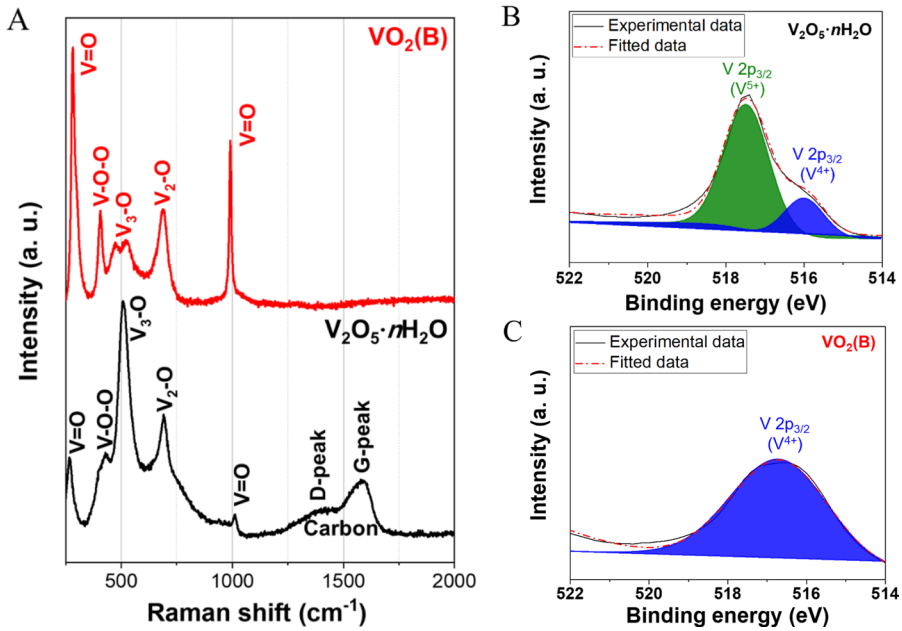

Fig. 5 Chemical characterization of the $V_2O_5{\cdot}nH_2O$ and VO_2(B) NBs; **a** Raman spectra of $V_2O_5{\cdot}nH_2O$ and VO_2(B) NBs. XPS spectra of **b** $V_2O_5{\cdot}nH_2O$ and **c** VO_2(B) NBs (V2p in the range of 512–522 eV)

which is consistent with our Raman observation. However, the compositions of the TCNC-based carbon in the $V_2O_5{\cdot}nH_2O$ and VO_2(B) NBs were analogous: the C1s spectrum of the $V_2O_5{\cdot}nH_2O$ NBs was deconvoluted as sp^2 (44%) at 284 eV, sp^3 (50%) at 285 eV, and C=O (6%) at 288 eV, and that of the VO_2(B) NBs was deconvoluted as sp^2 (39%), sp^3 (54%), and C=O (7%) (Ferrari and Robertson 2000). The atomic compositions of the $V_2O_5{\cdot}nH_2O$ and VO_2(B) NBs were examined by XPS surveys (Table 2).

Table 2 Atomic composition of $V_2O_5{\cdot}nH_2O$ and VO_2(B) NBs based on XPS surveys

Sample	C1s (%)	O1s (%)	V2p (%)	Total (%)
$V_2O_5{\cdot}nH_2O$	23.32	60.57	16.11	100
VO_2(B)	10.54	69.41	20.5	100

Electrochemical performance of vanadium oxide for Li ion batteries

Despite their high electronic conductivity of approximately 10^{-1} S/cm (Fu et al. 2013; Kinaci et al. 2015), VO_2(B) nanostructures are still beneficial in overcoming the inferior Li-ion diffusion behavior in the solid state with a diffusion coefficient of 10^{-15} cm^2/s (Gu et al. 2019) because of the short Li-ion diffusion pathway and efficient contact area of the electrode and electrolyte. In addition, designing VO_2(B) nanostructures with preferred orientation further facilitates the Li-ion intercalation/deintercalation because of the uniaxial Li-ion diffusion pathway parallel to the [001] crystal orientation (Li et al. 2017; Liu et al. 2017a; Xia et al. 2018). A hydrothermal process using V_2O_5 is an efficient route to synthesize a single-crystalline 1D VO_2(B) nanostructure (Zhang et al. 2006); however, achieving preferred orientation requires a reductive organic agent (polyethylene glycol) and extraordinarily long synthesis time of a few days (Li et al. 2013a; Liu et al. 2004). Thus, it is necessary to explore novel routes to synthesize the 1D VO_2(B) nanostructures with tunable crystal orientations and morphology while considerably reduced processing time for potential mass production.

The electrochemical performances of the $V_2O_5{\cdot}nH_2O$ and VO_2(B) NBs were examined using galvanostatic charge/discharge tests in the voltage range from 1.5 to 4 V at a current density of 1C. Figure 6a, b present the voltage profiles from the 1st to 10th cycles of the $V_2O_5{\cdot}nH_2O$ and VO_2(B) NBs electrodes. The initial discharge capacities of the $V_2O_5{\cdot}nH_2O$ and VO_2(B) NBs were 333.9 and 403.1 mAh/g, respectively. The discharge capacity of the $V_2O_5{\cdot}nH_2O$ NBs at the 10th cycle were reduced to 283.1 mAh/g, whereas that of the VO_2(B) NBs were less significantly reduced to 294.1 mAh/g.

The fact that the $V_2O_5{\cdot}nH_2O$ and VO_2(B) NBs have the layered structures formed by corner- and/or edge-sharing VO_6 octahedron along the *ab* plane, leading to efficient intercalation of Li ions. Such layered structure $V_2O_5{\cdot}nH_2O$ is a promising energy-storage material because of its very large d-spacing (≒11.8 Å) because H_2O molecules exist in the interlayer of the bilayer. However, VO_2(B) causes efficient diffusion of Li ions by 1D tunnels along the b axis, although the d-spacing is relatively narrow because that VO_2 (B) consists of two edge-sharing octahedra units. Figure S9 presents the ex-situ XRD curves of charged and discharged VO_2(B) and $V_2O_5{\cdot}nH_2O$ nanobelts at tenth cycle. The XRD curves of VO_2 nanobelts demonstrate a reversible reaction with unchanged peak positions, whereas the XRD curves of $V_2O_5{\cdot}nH_2O$ represent an irreversible crystallographic change with significant peak shifts. During lithiation, the crystal structure of $V_2O_5{\cdot}nH_2O$ undergoes a high angle shift as well as a phase transition to VO_2, originated from a reduction of interlayer distance by dehydration. This structural changes of $V_2O_5{\cdot}nH_2O$ to VO_2 are considered to be the cause of the similar working potentials shown in the dQ/dV in Fig. 6c. The Li intercalation mechanism of vanadium oxides is related not only to the crystal structure but also to the valence state of vanadium (V^{2+}, V^{3+}, V^{4+}, and V^{5+}). Li-ion diffusion fills the structure with Li ions owing to the high valence state of vanadium, and as the Li concentration increases, the valence state of vanadium gradually decreases. The increase in Li concentration due to diffusion of Li ions was investigated using differential capacity analysis. According to the first-principles calculation, it is known that Li intercalation in vanadium oxide appears from 2.3 to 2.7 V (Li et al. 2017). VO_2 crystal structure has several Li-ion sites, including A1, A2, C, and C'. At low Li concentration ($0 < x < 0.25$, Li_xVO_2), voltage plateaus at around 2.7 V corresponds to Li occupation

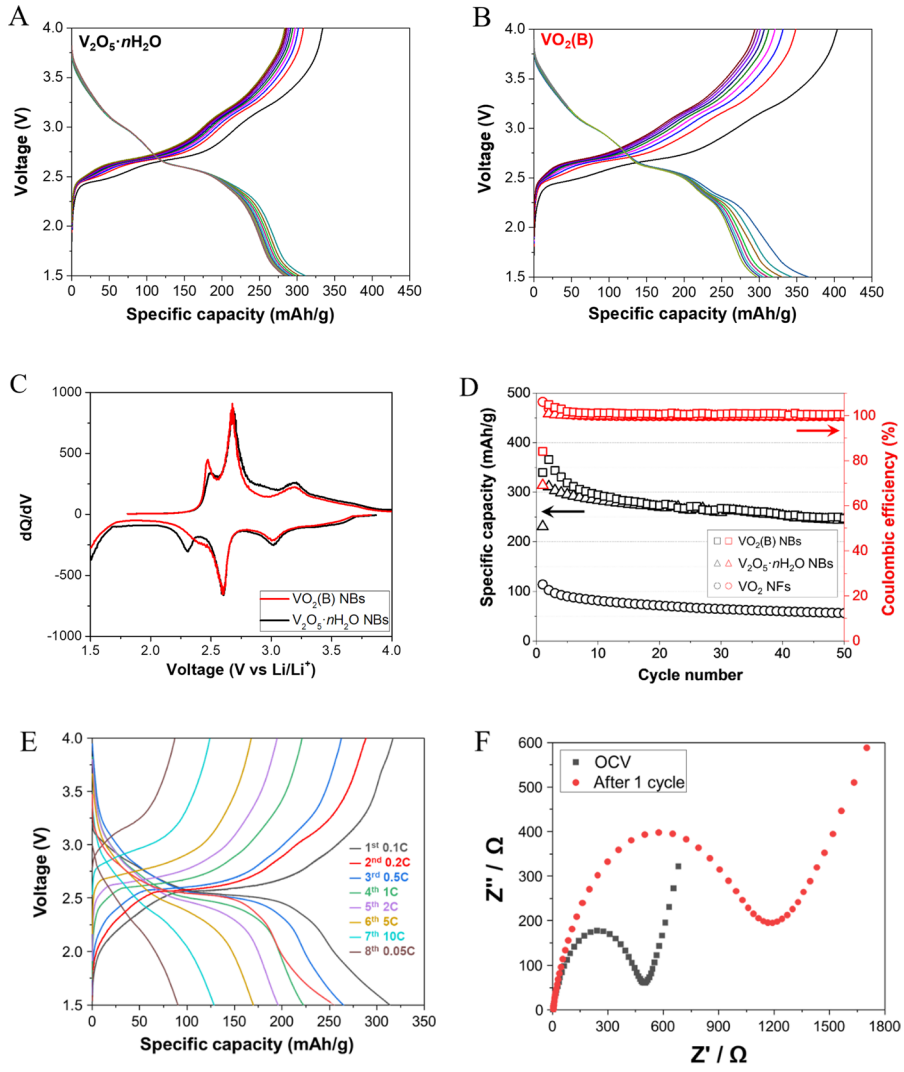

Fig. 6 Electrochemical characterization of the $V_2O_5{\cdot}nH_2O$ and VO_2(B) NBs. Charge/discharge voltage profile of **a** $V_2O_5{\cdot}nH_2O$ and **b** VO_2(B) NBs at 1C over the potential range 1.5–4.0 V vs. Li + /Li in 1–10 cycles. **c** Differential capacity (dQ/dV) plots of $V_2O_5{\cdot}nH_2O$ and VO_2(B) NBs for 1st cycle. The redox potential peaks of VO_2(B) and $V_2O_5{\cdot}nH_2O$ were evolved at 3.19, 2.68, and 2.47 V for the cathodic process, and around 3.00, 2.59, and 2.30 V for the anodic process. **d** Electrochemical performance plots of specific discharge capacity for 50 cycles of VO_2 NFs, $V_2O_5{\cdot}nH_2O$ NBs and VO_2(B) NBs. **e** Charge–discharge curve of VO_2(B) NBs at different current densities. **f** AC impedance plots of VO_2(B) NBs in the range from 0.1 Hz to 100 kHz

at the C site by partially reducing V^{4+} to V^{3+}. At high Li concentration ($0.25 < x < 1.0$, Li_xVO_2), A1 and A2 sites are occupied by Li-ion with full reduction of V^{4+} to V^{3+} in the potential range between 2.57 and 2.38 V. The redox reaction that occurs in the high voltage range (3.0 ~ 3.2 V) is related to $Li_xV_2O_5$ and is presumed to be a reaction involving by-products such as single-crystal VO_2(B) and $V_2O_5{\cdot}nH_2O$ that have been synthesized (Yuhan et al. 2019; Felix et al. 2017). Characteristic redox peaks of the VO_2(B) were developed at approximately 2.6 V, and the irreversible redox peaks, considered as the pseudocapacitive behavior, were more significantly developed in the initial differential capacity curve of VO_2(B) (approximately 2.3 V) (Liu et al. 2017c; Xia et al. 2018). Thus, the reversible discharge capacity of the $V_2O_5{\cdot}nH_2O$ and VO_2(B) NBs at the 50th cycle was greater than 240 mAh/g, which is comparable to that of commercial lithium transition-metal oxide and phosphate cathode materials (Fig. 6d). Furthermore, $V_2O_5{\cdot}nH_2O$ and VO_2(B) NBs exhibited a relatively low Coulomb efficiency of 69.0% and 84.1%, respectively, but except for first cycle, they showed a high Coulomb efficiency of over 99%. The galvanostatic charge–discharge curves of the VO_2(B) NBs under various C-rates are presented in Fig. 6e. The reversible discharge capacities of the VO_2(B) NBs were 313, 264, 222, 195, 169, 128, 90, and 254 mAh/g at 0.1, 0.2, 0.5, 1C, 2C, 5C, 10C, and 0.05C, respectively. Figure 6f presents AC impedance plots of the VO_2(B)

NBs at OCV and after charge–discharge for 1 cycle. The diameter of the semicircles corresponding to the charge-transfer resistance increased after 1 cycle, which can be attributed to the effect of the crystal structure under Li intercalation/deintercalation.

The electrochemical performance of the VO_2(B) NBs in this work and of previously reported VO_2(B) nanostructures are summarized in Table 3. The reversible capacity and cycling performances of the VO_2(B) NBs in this work were clearly much greater than those of the previously reported VO_2(B) nanostructures. This enhanced performance can be attributed to the synergistic effect of the single-crystalline structure and residual carbonaceous elements for NVOs NBs. The single-crystalline cathode materials are beneficial from good capacity retention due to structural stability (Kimijima et al. 2016; Chen et al. 2019; Xu et al. 2019), and a small amount of residual carbonaceous materials may be facilitative to the charge transfer (Dong et al. 2019). Thus, it can be concluded that the VO_2(B) NBs synthesis using the TCNC templates is extremely effective for the manufacture of promising vanadium-based cathode materials with single-crystalline structure and excellent electrochemical performance.

Conclusions

In summary, vanadium oxide was prepared using TCNCs templated hydrothermal synthesis. The main variables in the hydrothermal synthesis process are the amount of TCNCs added to the precursor and the process temperature, and various crystalline- and morphological- NVOs were synthesized depending

Table 3 Electrochemical behavior of 1D nanostructure VO_2(B) as a cathode material for LIBs

Active material	Shape	Voltage range (V)	Cycle number	1st cycle discharge capacity	Last cycle discharge capacity	Electrode composition	References
Single- crystalline VO_2(B)	Nanobelts	1.5–4	50	348 mAh/g at 1C	244 mAh/g at 1C	VO_2 (80):Super P (10):PVDF (10)	This work
Single-crystalline VO_2(B)	Nanorods	1.5–3.5	17	152 mAh/g at 1C	75 mAh/g at 1C	VO_2 (75):acetylene black (20):PTFE (5)	Subba Reddy et al. (2009)
Polycrystalline VO_2(B)	Nanorods	1.5–4	47	171 mAh/g at 1C	108 mAh/g at 1C	VO_2 (70):acetylene black (20):PVDF (10)	Ganganagappa and Siddaramanna (2012)
Single-crystalline VO_2(B)	Nanorods	2.0–3.6	100	195 mAh/g at 30 mA/g	130 mAh/g at 30 mA/g	VO_2 (80):carbon black (15):PVDF (5)	Liu et al. (2017b)
VO_2(B)	Nanobelts	1.5–3.75	2	316 mAh/g at 214 mA/g	323 mAh/g at	VO_2 (80):acetylene black (10) :PVDF (10)	Ni et al. (2011)
VO_2(B)	Nanoflowers	0.01–4	30	206.8 mAh/g at 40 mA/g	6.5 mAh/g at 40 mA/g	VO_2 (80):Super P (10):PVDF (10)	Fan et al. (2016)
VO_2(B)	Nanobelts	2–3	100	158 mAh/g at 100 mA/g	134 mAh/g at 100 mA/g	VO_2 (70):acetylene black (20):PTFE (10)	Mai et al. (2013)

on the process conditions. Moreover, the structural analysis reveal that the aspect ratios decreased as the amount of TCNCs increased in the hydrothermal synthesis process. Among the various NVOs, $V_2O_5{\cdot}nH_2O$ and VO_2(B) NBs were applied as energy storage materials through a large path for ion inside the crystal structure. Through electrochemical analysis, single crystalline $V_2O_5{\cdot}nH_2O$ and VO_2(B) NBs with the preferred crystal orientation were compared with polycrystalline VO_2(B) NFs. The efficient Li ion path of the single crystalline $V_2O_5{\cdot}nH_2O$ and VO_2(B) NBs was demonstrated by high specific capacity and long cycling performance through the charge/discharge profile. As a result, we conclude that TCNC-templated hydrothermal synthesis is effective way to prepare the single-crystalline NVOs for a short processing time, and such the single-crystalline NVOs exhibited excellent performance as a cathode of a LIBs.

Acknowledgments This research was partly supported by Basic Science Research Program through the National Research Foundation of Korea (NRF) (NRF-2020R1A6A1A03043435, NRF-2021R1A2C2010781) and Korea Institute for Advancement of Technology(KIAT) grant funded by the Korea Government(MOTIE) ((P0023521, HRD Program for Industrial Innovation). J.L. was supported in part by the DGIST R&D Program of the Ministry of Science, ICT and Future Planning, Korea (23-IT-02).

Author's contributions All authors contributed to the study conception and design. CY and WK have contributed to this work equally, as co-first authors. Material preparation, data collection and analysis were performed by CY and WK, CY and WK wrote the first draft of the manuscript and TC reviewed the manuscript and supervised all experimental works. All authors have read and approved to the published version of the final manuscript.

Data availability None.

Declarations

Conflict of interest All authors declare no conflicts of interest.

Consent for publication All authors consent to publishing this work.

Ethics approval The authors confirm that there were no ethical in preparing this manuscript and consent to participating in this work.

References

Ahmed SE, Adrew JP, Peter S, Niklas H, Xiaodong Z, Junliang S, Diana B (2019) Insights into the exfoliation process of $V_2O_5{\cdot}nH_2O$ nanosheet formation using real-time ^{51}V NMR. ACS Omega 4:10899–10905. https://doi.org/10.1021/acsomega.9b00727

Arcangeletti E, Baldassarre L, Di Castro D, Lupi S, Malavasi L, Marini C, Perucchi A, Postorino P (2007) Evidence of a pressure-induced metallization process in monoclinic VO_2. Phys Rev Lett 98(19):196406. https://doi.org/10.1103/PhysRevLett.98.196406

Bahlawane N, Lenoble D (2014) Vanadium oxide compounds:structure, properties, and growth from the gas phase. Chem Vapor Depos 20:299–311. https://doi.org/10.1002/cvde.201400057

Chen G, Zhu J (2019) Single-crystal based studies for correlating the properties and high-voltage performance of $Li[Ni_xMn_yCo_{1-x-y}]O_2$ cathodes. J Mater Chem A 7:5463–5474. https://doi.org/10.1039/C8TA10329A

Chen M, Liang X, Wang F, Xie D, Pan G, Xia X (2019) Self-supported VO_2 arrays decorated with N-doped carbon as an advanced cathode for lithium-ion storage. J Mater Chem A 7(12):6644–6650. https://doi.org/10.1039/c8ta11578h

Cui F, Zhao J, Zhang D, Fang Y, Hu F, Zhu K (2020) VO_2(B) nanobelts and reduced graphene oxides composites as cathode materials for low-cost rechargeable aqueous zinc ion batteries. Chem Eng J. https://doi.org/10.1016/j.cej.2020.124118

De France K, Zeng Z, Wu T, Nyström G (2021) Functional materials from nanocellulose: utilizing structure–property relationships in bottom-up fabrication. Adv Mater 33(28):2000657. https://doi.org/10.1002/adma.202000657

Dong H, Liu G, Li S, Deng S, Cui Y, Liu H, Liu H, Sun X (2019) Design of a 3D-porous structure with residual carbon for high-performance Ni-rich cathode materials. ACS Appl Mater Interfaces 11(2):2500–2506. https://doi.org/10.1021/acsami.8b17800

Eyley S, Thielemans W (2014) Surface modification of cellulose nanocrystals. Nanoscale 6(14):7764–7779. https://doi.org/10.1039/c4nr01756k

Fan Z, Jia L, Lin C, Huang X, Hu X, Zhuang N, Chen J (2016) Enhanced electrochemical performance of vanadium dioxide (B) nanoflowers with graphene nanoribbons support. RSC Adv 6(16):13297–13302. https://doi.org/10.1039/c5ra20018k

Felix M, Kobe G, Geert R, Jolien D, Christophe D (2017) Amorphous and crystalline vanadium oxides as high-energy and high-power cathodes for three-dimensional thin-film lithium ion batteries. ACS Appl Mater Interfaces 9(15):13121–13131. https://doi.org/10.1021/acsami.6b16473

Ferrari AC, Robertson J (2000) Interpretation of Raman spectra of disordered and amorphous carbon. Phys Rev B 61(20):14095. https://doi.org/10.1103/PhysRevB.61.14095

Fu D, Liu K, Tao T, Lo K, Cheng C, Liu B, Zhang R, Bechtel HA, Wu J (2013) Comprehensive study of the

metal-insulator transition in pulsed laser deposited epitaxial VO_2 thin films. J Appl Phys. https://doi.org/10.1063/1.4788804

Ganganagappa N, Siddaramanna A (2012) One step synthesis of monoclinic VO_2 (B) bundles of nanorods: Cathode for Li ion battery. Mater Charact 68:58–62. https://doi.org/10.1016/j.matchar.2012.03.010

Gu L, Wang J, Ding J, Li B, Yang S (2019) W-doped VO_2(B) nanosheets-built 3D networks for fast lithium storage at high temperatures. Electrochim Acta 295:393–400. https://doi.org/10.1016/j.electacta.2018.10.145

He G, Li L, Manthiram A (2015) VO_2/rGO nanorods as a potential anode for sodium- and lithium-ion batteries. J Mater Chem A 3(28):14750–14758. https://doi.org/10.1039/c5ta03188e

Hu B, Li L, Xiong X, Liu L, Huang C, Yu D, Chen C (2019) High-performance of copper-doped vanadium pentoxide porous thin films cathode for lithium-ion batteries. J Solid State Electrochem 23(5):1315–1324. https://doi.org/10.1007/s10008-019-04220-w

Jeon DH, Baek SM (2011) Thermal modeling of cylindrical lithium ion battery during discharge cycle. Energy Convers Manag 52(8–9):2973–2981. https://doi.org/10.1016/j.enconman.2011.04.013

Kang Q, Zhang Y, Bao S, Zhang G (2019) Eco-friendly synthesis of VO_2 with stripped pentavalent vanadium solution extracted from vanadium-bearing shale by hydrothermal process in high conversion rate. R Soc Open Sci 6(2):181116. https://doi.org/10.1098/rsos.181116

Kimijima T, Zettsu N, Yubuta K, Hirata K, Kami K, Teshima K (2016) Molybdateflux growth of idiomorphic $Li(Ni_{1/3}Co_{1/3}Mn_{1/3})O_2$ single crystals and characterization oftheir capabilities as cathode materials for lithium-ion batteries. J Mater Chem A 4:7289–7296. https://doi.org/10.1039/C6TA01593J

Kinaci A, Kado M, Rosenmann D, Ling C, Zhu G, Banerjee D, Chan MKY (2015) Electronic transport in VO_2 Experimentally calibrated Boltzmann transport modeling. Appl Phys Lett 10(1063/1):4938555

Kramer D, Ceder G (2009) Tailoring the morphology of $LiCoO_2$: a first principles study. Chem Mater 21(16):3799–3809. https://doi.org/10.1021/cm9008943

Lamm ME, Li K, Qian J, Wang L, Lavoine N, Newman R, Gardner DJ, Li T, Hu L, Ragauskas AJ (2021) Recent advances in functional materials through cellulose nanofiber templating. Adv Mater 33(12):2005538. https://doi.org/10.1002/adma.202005538

Lavoine N, Bergström L (2017) Nanocellulose-based foams and aerogels: processing, properties, and applications. J Mater Chem A 5(31):16105–16117. https://doi.org/10.1039/C7TA02807E

Lazzarini A, Piovano A, Pellegrini R, Leofanti G, Agostini G, Rudić S, Chierotti MR, Gobetto R, Battiato A, Spoto G, Zecchina A, Lamberti C, Groppo E (2016) A comprehensive approach to investigate the structural and surface properties of activated carbons and related Pd-based catalysts. Catal Sci Technol 6(13):4910–4922. https://doi.org/10.1039/c6cy00159a

Lee MJ, Lee S, Oh P, Kim Y, Cho J (2014) High performance $LiMn_2O_4$ cathode materials grown with epitaxial layered nanostructure for Li-ion batteries. Nano Lett 14(2):993–999. https://doi.org/10.1021/nl404430e

Lee S, Ivanov IN, Keum JK, Lee HN (2016) Epitaxial stabilization and phase instability of VO_2 polymorphs. Sci Rep 6:19621. https://doi.org/10.1038/srep19621

Li B, Ni X, Zhou F, Cheng J, Zheng H, Ji M (2006) A facile surfactant-free method to the synthesis of tip-ended VO_2 nanorods in high yield. Solid State Sci 8(10):1168–1172. https://doi.org/10.1016/j.solidstatesciences.2006.05.003

Li H, He P, Wang Y, Hosono E, Zhou H (2011) High-surface vanadium oxides with large capacities for lithium-ion batteries: from hydrated aerogel to nanocrystalline VO_2(B), V_6O_{13} and V_2O_5. J Mater Chem. https://doi.org/10.1039/c1jm11523e

Li M, Li D-B, Pan J, Lin J-C (2013a) Li G-H (2013a) selective synthesis of vanadium oxides and investigation of the thermochromic properties of VO_2 by infrared spectroscopy. Eur J Inorg Chem 7:1207–1212. https://doi.org/10.1002/ejic.201201118

Li N, Huang W, Shi Q, Zhang Y, Song L (2013b) A CTAB-assisted hydrothermal synthesis of VO_2(B) nanostructures for lithium-ion battery application. Ceram Int 39(6):6199–6206. https://doi.org/10.1016/j.ceramint.2013.01.039

Li S, Liu J-B, Wan Q, Xu J, Liu B-X (2017) First-principles analysis of Li intercalation in VO_2(B). Chem Mater 29(23):10075–10087. https://doi.org/10.1021/acs.chemmater.7b03750

Liang L, Liu H, Yang W (2013) Fabrication of VO_2(B) hybrid with multiwalled carbon nanotubes to form a coaxial structure and its electrochemical capacitance performance. J Alloy Compd 559:167–173. https://doi.org/10.1016/j.jallcom.2013.01.111

Lin N, Bruzzese C, Dufresne A (2012) TEMPO-oxidized nanocellulose participating as crosslinking aid for alginate-based sponges. ACS Appl Mater Interfaces 4(9):4948–4959. https://doi.org/10.1021/am301325r

Liu J, Li Q, Wang T, Yu D, Li Y (2004) Metastable vanadium dioxide nanobelts: hydrothermal synthesis, electrical transport, and magnetic properties. Angew Chem Int Ed Engl 43(38):5048–5052. https://doi.org/10.1002/anie.200460104

Liu H, Wang Y, Wang K, Hosono E, Zhou H (2009) Design and synthesis of a novel nanothorn VO_2(B) hollow microsphere and their application in lithium-ion batteries. J Mater Chem. https://doi.org/10.1039/b821799h

Liu L, Liu Q, Zhao W, Li G, Wang L, Shi W, Chen L (2017a) Enhanced electrochemical performance of orientated VO_2(B) raft-like nanobelt arrays through direct lithiation for lithium ion batteries. Nanotechnology 28(6):065404. https://doi.org/10.1088/1361-6528/aa521a

Liu M, Su B, Tang Y, Jiang X, Yu A (2017b) Resent advances in nanostructred vanadium oxides and composites for energy conversion. Adv Energy Mater 7:1700885. https://doi.org/10.1002/aenm.201700885

Liu Q, Tan G, Wang P, Abeyweera SC, Zhang D, Rong YA, Wu Y, Lu J, Sun C-J, Ren Y, Liu Y, Muehleisen RT, Guzowski LB, Li J, Xiao X, Sun Y (2017c) Revealing mechanism responsible for structural reversibility of single-crystal VO_2 nanorods upon lithiation/delithiation.

Nano Energy 36:197–205. https://doi.org/10.1016/j.nanoen.2017.04.023

Liu Y, Shi T, Zhang T, Yuan D, Peng Y, Qiu F (2019) Cellulose-derived multifunctional nano-CuO/carbon aerogel composites as a highly efficient oil absorbent. Cellulose 26(9):5381–5394. https://doi.org/10.1007/s10570-019-02484-z

Livage J (2010) Hydrothermal synthesis of nanostructured vanadium oxides. Materials 3(8):4175–4195. https://doi.org/10.3390/ma3084175

Lübke M, Ding N, Powell MJ, Brett DJL, Shearing PR, Liu Z, Darr JA (2016) VO_2 nano-sheet negative electrodes for lithium-ion batteries. Electrochem Commun 64:56–60. https://doi.org/10.1016/j.elecom.2016.01.013

Mai L, Wei Q, An Q, Tian X, Zhao Y, Xu X, Xu L, Chang L, Zhang Q (2013) Nanoscroll buffered hybrid nanostructural VO_2(B) cathodes for high-rate and long-life lithium storage. Adv Mater 25(21):2969–2973. https://doi.org/10.1002/adma.201205185

Merindol R, Diabang S, Mujica R, Le Houerou V, Roland T, Gauthier C, Decher G, Felix O (2020) Assembly of anisotropic nanocellulose films stronger than the original tree. ACS Nano 14(12):16525–16534. https://doi.org/10.1021/acsnano.0c01372

Moon RJ, Martini A, Nairn J, Simonsen J, Youngblood J (2011) Cellulose nanomaterials review: structure, properties and nanocomposites. Chem Soc Rev 40(7):3941–3994. https://doi.org/10.1039/c0cs00108b

Ni S, Zeng H, Yang X (2011) Fabrication of VO_2(B) nanobelts and their application in lithium ion batteries. J Nanomater 2011:1–4. https://doi.org/10.1155/2011/961389

Okita Y, Saito T, Isogai A (2010) Entire surface oxidation of various cellulose microfibrils by TEMPO-mediated oxidation. Biomacromol 11(6):1696–1700. https://doi.org/10.1021/bm100214b

Perera SD, Patel B, Bonso J, Grunewald M, Ferraris JP, Balkus KJ (2011) Vanadium oxide nanotube spherical clusters prepared on carbon fabrics for energy storage applications. ACS Appl Mater Interfaces 3(11):4512–4517. https://doi.org/10.1021/am2011965

Petkov V, Trikalitis PN, Bozin ES, Billinge SJ, Vogt T, Kanatzidis MG (2002) Structure of V_2O_5·n H_2O xerogel solved by the atomic pair distribution function technique. J Am Chem Soc 124(34):10157–10162. https://doi.org/10.1021/ja026143y

Popuri SR, Miclau M, Artemenko A, Labrugere C, Villesuzanne A, Pollet M (2013) Rapid hydrothermal synthesis of VO_2(B) and its conversion to thermochromic VO_2(M1). Inorg Chem 52(9):4780–4785. https://doi.org/10.1021/ic301201k

Prześniak-Welenc M, Karczewski J, Smalc-Koziorowska J, Łapiński M, Sadowski W, Kościelska B (2016) The influence of nanostructure size on V_2O_5 electrochemical properties as cathode materials for lithium ion batteries. RSC Adv 6(61):55689–55697. https://doi.org/10.1039/c6ra05695d

Qiao Y, Deng H, He P, Zhou H (2020) A 500 Wh/kg lithium-metal cell based on anionic redox. Joule 4(7):1445–1458. https://doi.org/10.1016/j.joule.2020.05.012

Rahman MM, Wang J-Z, Idris NH, Chen Z, Liu H (2010) Enhanced lithium storage in a VO_2(B)-multiwall carbon nanotube microsheet composite prepared via an in situ hydrothermal process. Electrochim Acta 56(2):693–699. https://doi.org/10.1016/j.electacta.2010.10.012

Saji VS, Kim YS, Kim TH, Cho J, Song HK (2011) One-dimensional (1D) nanostructured and nanocomposited $LiFePO_4$: its perspective advantages for cathode materials of lithium ion batteries. Phys Chem Chem Phys 13(43):19226–19237. https://doi.org/10.1039/c1cp22818h

Salah M, Azizi S, Boukhachem A, Khaldi C, Amlouk M, Lamloumi J (2019) Rietveld refinement of X-ray diffraction, impedance spectroscopy and dielectric relaxation of Li-doped ZnO-sprayed thin films. Appl Phys A 125:615. https://doi.org/10.1007/s00339-019-2911-3

Sevilla M, Fuertes AB (2009) The production of carbon materials by hydrothermal carbonization of cellulose. Carbon 47(9):2281–2289. https://doi.org/10.1016/j.carbon.2009.04.026

Shinoda R, Saito T, Okita Y, Isogai A (2012) Relationship between length and degree of polymerization of TEMPO-oxidized cellulose nanofibrils. Biomacromol 13(3):842–849. https://doi.org/10.1021/bm2017542

Simões M, Surace Y, Yoon S, Battaglia C, Pokrant S, Weidenkaff A (2015) Hydrothermal vanadium manganese oxides: anode and cathode materials for lithium-ion batteries. J Power Sour 291:66–74. https://doi.org/10.1016/j.jpowsour.2015.04.156

Subba Reddy CV, Walker EH, Wicker SA, Williams QL, Kalluru RR (2009) Synthesis of VO_2(B) nanorods for Li battery application. Curr Appl Phys 9(6):1195–1198. https://doi.org/10.1016/j.cap.2009.01.012

Sudant G, Baudrin E, Dunn B, Tarascon J-M (2004) Synthesis and electrochemical properties of vanadium oxide aerogels prepared by a freeze-drying process. J Electrochem Soc. https://doi.org/10.1149/1.1687427

Sun J, Zhang Y, Liu Y, Jiang H, Dong X, Hu T, Meng C (2021) Hydrated vanadium pentoxide/reduced graphene oxide-polyvinyl alcohol ($V_2O_5nH_2O$/rGO-PVA) film as a binder-free electrode for solid-state Zn-ion batteries. J Colloid Interface Sci 587:845–854. https://doi.org/10.1016/j.jcis.2020.10.148

Susai FA, Sclar H, Shilina Y, Penki TR, Raman R, Maddukuri S, Maiti S, Halalay IC, Luski S, Markovsky B, Aurbach D (2018) Horizons for Li-ion batteries relevant to electromobility: high-specific-energy cathodes and chemically active separators. Adv Mater 30(41):e1801348. https://doi.org/10.1002/adma.201801348

Toby BH (2006) R factors in Rietveld analysis: how good is good enough? Powder Diffr 21(1):67–70. https://doi.org/10.1154/1.2179804

Wang Y, Shang H, Chou T, Cao G (2005) Effects of thermal annealing on the Li^+ intercalation properties of V_2O_5·n H_2O xerogel films. J Phys Chem B 109(22):11361–11366. https://doi.org/10.1021/jp051275+

Wang H, Yi H, Chen X, Wang X (2014) One-step strategy to three-dimensional graphene/VO_2 nanobelt composite hydrogels for high performance supercapacitors. J Mater Chem A 2(4):1165–1173. https://doi.org/10.1039/c3ta13932h

Wang X, Yao C, Wang F, Li Z (2017) Cellulose-based nanomaterials for energy applications. Small 13(42):1702240. https://doi.org/10.1002/smll.201702240

Wang G, Bi X, Yue H, Jin R, Wang Q, Gao S, Lu J (2019) Sacrificial template synthesis of hollow C@ MoS_2@ PPy nanocomposites as anodes for enhanced sodium storage performance. Nano Energy 60:362–370. https://doi.org/10.1016/j.nanoen.2019.03.065

Wei Q, Liu J, Feng W, Sheng J, Tian X, He L, An Q, Mai L (2015) Hydrated vanadium pentoxide with superior sodium storage capacity. J Mater Chem A 3(15):8070–8075. https://doi.org/10.1039/c5ta00502g

Wu Z, Han X, Zheng J, Wei Y, Qiao R, Shen F, Dai J, Hu L, Xu K, Lin Y, Yang W, Pen F (2014) Depolarized and fully active cathode based on $Li(Ni_{0.5}Co_{0.2}Mn_{0.3})O_2$ embedded in carbon nanotube network for advanced batteries. Nanoletter 14(8):4700–4706. https://doi.org/10.1021/nl5018139

Xia C, Lin Z, Zhou Y, Zhao C, Liang H, Rozier P, Wang Z, Alshareef HN (2018) Large intercalation pseudocapacitance in 2D VO_2(B): breaking through the kinetic barrier. Adv Mater. https://doi.org/10.1002/adma.201803594

Xu X, et al (2012) Topotactically synthesized ultralong LiV_3O_8 nanowire cathode materials for high rate and long life rechargeable lithium batteries. NPG Asia Mater 4:e20. https://doi.org/10.1038/am.2012.36

Xu X, Huo H, Jian J, Wang L, Zhu H, Xu S, He X, Yin G, Du C, Sun X (2019) Radially oriented single-crystal primary nanosheets enable ultrahigh rate and cycling properties of $LiNi_{0.8}Co_{0.1}Mn_{0.1}O_2$ cathode material for lithium-ion batteries. Adv Energy Mater 9:1803963. https://doi.org/10.1002/aenm.201803963

Xu T, Du H, Liu H, Liu W, Zhang X, Si C, Liu P, Zhang K (2021) Advanced nanocellulose-based composites for flexible functional energy storage devices. Adv Mater 33(48):2101368. https://doi.org/10.1002/adma.202101368

Yamaguchi M, Manaf MEA, Songsurang K, Nobukawa S (2012) Material design of retardation films with extraordinary wavelength dispersion of orientation birefringence: a review. Cellulose 19(3):601–613. https://doi.org/10.1007/s10570-012-9660-1

Yang X, Biswas SK, Han J, Tanpichai S, Li MC, Chen C, Zhu S, Das AK, Yano H (2021) Surface and interface engineering for nanocellulosic advanced materials. Adv Mater 33(28):2002264. https://doi.org/10.1002/adma.202002264

Youn C, Bae YH, Kim WS, Yeo SY (2021) Research for mechanical properties of wet nonwoven fabric based on recycled carbon fiber using cellulose nanofibrils. Textile Sci Eng 58(1):40–47

Youn C, Shin S, Shin K, Kim C, Park CL, Choi J, Kim SH, Yeo SY, Shin MW, Henkelman G, Yoon KR (2022) Template-assisted synthesis of single-atom catalysts supported on highly crystalline vanadium pentoxide for stable oxygen evolution. Chem Catal 2:1–20. https://doi.org/10.1016/j.checat.2022.03.017

Yuhan J, Xiaowei Z, Xu C, Jia W, Linlin G, Mingxia S, Yang R, Zhu L (2019) Controlled hydrothermal growth and Li storage performance of 1D VOx nanobelts with variable vanadium valence. Nanomaterials 9(4):624. https://doi.org/10.3390/nano9040624

Zhang K-F, Bao S-J, Liu X, Shi J, Su Z-X, Li H-L (2006) Hydrothermal synthesis of single-crystal VO_2(B) nanobelts. Mater Res Bull 41(11):1985–1989. https://doi.org/10.1016/j.materresbull.2006.07.001

Zhang S, Chou JY, Lauhon LJ (2009) Direct correlation of structural domain formation with the metal insulator transition in a VO_2 nanobeam. Nano Lett 9(12):4527–4532. https://doi.org/10.1021/nl9028973

Zhang Y, Xiong W, Chen W, Zheng Y (2021) Recent progress on vanadium dioxide nanostructures and devices: fabrication, properties, applications and perspectives. Nanomaterials 11:338. https://doi.org/10.3390/nano11020338

Zhao Y, Han C, Yang J, Su J, Xu X, Li S, Xu L, Fang R, Jiang H, Zou X, Song B, Mai L, Zhang Q (2015) Stable alkali metal ion intercalation compounds as optimized metal oxide nanowire cathodes for lithium batteries. Nano Lett 15(3):2180–2185. https://doi.org/10.1021/acs.nanolett.5b00284

Zhao J, Ren H, Liang Q, Yuan D, Xi S, Wu C, Manalastas W, Ma J, Fang W, Zheng Y, Du C-F, Srinivasan M, Yan Q (2019) High-performance flexible quasi-solid-state zinc-ion batteries with layer-expanded vanadium oxide cathode and zinc/stainless steel mesh composite anode. Nano Energy 62:94–102. https://doi.org/10.1016/j.nanoen.2019.05.010